BIOCHEMISTRY
including biophysical chemistry & molecular biology
Article

Biochemistry **2010,** *49,* 4181–4190 4181
DOI: 10.1021/bi9021236

Crosstalk along the Stalk: Dynamics of the Interaction of Subunits B and F in the A_1A_O ATP Synthase of *Methanosarcina mazei* Gö1†

Devanathan Raghunathan,‡ Shovanlal Gayen,§ Gerhard Grüber,*,‡,§ and Chandra S. Verma*,‡,§,∥

‡*Bioinformatics Institute (A*STAR), 30 Biopolis Street, #07-01 Matrix, Singapore 138671,* §*School of Biological Sciences, Nanyang Technological University, 60 Nanyang Drive, Singapore 637551, and* ∥*Department of Biological Sciences, National University of Singapore, 14 Science Drive 4, Singapore 117543*

Received December 10, 2009; Revised Manuscript Received April 7, 2010

ABSTRACT: The mechanism of coupling of ion pumping in the membrane-bound A_O sector with ATP synthesis in the A_3B_3 headpiece of the A_1 sector in the A_1A_O ATP synthase is a puzzle. Previously, crosstalk between the stalk and nucleotide-binding subunits F_{Mm} and B_{Mm} of the *Methanosarcina mazei* Gö1 A-ATP synthase has been observed by nucleotide-dependent cross-link formation of both subunits inside the enzyme. The recently determined NMR solution structure of F_{Mm} depicts the protein as a two-domain structure, with a well-folded N-terminus having 78 residues and a flexible C-terminal part (residues 79−101), proposed to become structured after binding to its partner, B_{Mm}. Here, we detail the crucial interactions between subunits B_{Mm} and F_{Mm} by determining the NMR structure of the very C-terminus of F_{Mm}, consisting of 20 residues and hereafter termed $F_{Mm(81-101)}$, and performing molecular dynamics simulations on the resulting structure. These data demonstrate that the flexibility of the C-terminus enables F_{Mm} to switch between an elongated and retracted state. Docking and MD in conjunction with previously conducted and published NMR results, biochemical cross-linking, and fluorescence spectroscopy data were used to reconstruct a model of a B_{Mm}−F_{Mm} assembly. The model of the B_{Mm}−F_{Mm} complex shows the detailed interactions of helices 1 and 2 of the C-terminal domain of B_{Mm} with the C-terminal residues of F_{Mm}. Movements of both helices of B_{Mm} accommodate the incoming C-terminus of F_{Mm} and connect the events of ion pumping and nucleotide binding in the A_1A_O ATP synthase.

The A_1A_O ATP synthase is the enzyme responsible for the synthesis of ATP from ADP and an inorganic phosphate in archaea such as methanogens (*1*). This enzyme is composed of 10 subunits in a proposed A_3:B_3:C:D:E:F:G:H_2:*a*:c_x stoichiometry (*2*). The A_1A_O ATP synthase is functionally related to the F_1F_O ATP synthase from eukaryotes and prokaryotes (*2*, *3*). Like other members of the larger family, the A_1A_O ATP synthase is divided into two parts: an integral membrane part, A_O, generating the ion gradient and a water-soluble part, A_1, which is the primary site for ATP synthesis (Figure 1). A_1 further consists of a hexameric A_3B_3 domain that spans ~96 Å in length with catalytic subunit A and the nucleotide-binding, noncatalytic subunit B arranged in an alternating manner (*4*, *5*). The central stalk, which is made up of subunits C, D, and F, functions as an elongated anchor that connects hexameric headpiece A_1 and membrane-embedded A_O, thus allowing for the energy to be transmitted by ion transduction from A_O to the A_1 sector (*6*−*8*). Details of the conformational and energetic coupling, caused by ion transduction in the A_O subunits as well as nucleotide binding and ATP synthesis in the A_3B_3 headpiece, remain sketchy notably because of the absence of atomistic detailed pictures of the stalk moiety that connects the two parts of the enzyme. Recently, the locations of ADP and ATP have been described in crystallographic structures of subunit B of the A_1A_O ATP synthase from *Methanosarcina mazei* Gö1 (B_{Mm}), revealing how the ATP traverses the protein surface to its final binding pocket and the concomitant rearrangements in the nucleotide-binding and C-terminal domain of B_{Mm} (*9*, *10*) (Figure 1). In addition, depending on whether MgATP or the nonhydrolyzable ATP analogue, MgAMP-PNP, is bound to B_{Mm}, a zero-length cross-link between B_{Mm} and subunit F (F_{Mm}) can be formed inside the methanogenic A_3B_3DF subcomplex (*4*), A_1 ATPase (*11*), and the A_1A_O ATP synthase (*12*), revealing their spatial proximity. Further, intrinsic tryptophan measurements demonstrate that recombinant B_{Mm} and F_{Mm} of the *M. mazei* Gö1 A-ATP synthase assemble with a binding constant of 322 nM, bringing tryptophan residues 430 and 100 of B_{Mm} and F_{Mm}, respectively, into the proximity of each other (*13*). F_{Mm} consists of a well-structured N-terminal domain and a flexible, partially ordered C-terminus (Figure 1). It is proposed that this flexibility enables F_{Mm} to undergo up and down movements relative to B_{Mm}, resulting in extended and retracted forms of F_{Mm} (*12*, *13*).

This study aims to explore the structural dynamics and underlying energetics of the interactions between B_{Mm} and F_{Mm} of the A_1A_O ATP synthase of *M. mazei* Gö1. We provide here, for the first time, a detailed picture of how the C-terminal stalk of F_{Mm} and the nucleotide-binding B_{Mm} of this enzyme interact with each other and how this interaction partially accomplishes coupling between the two motor elements, A_1 and A_O.

MATERIALS AND METHODS

Peptide Synthesis. Peptide $F_{Mm(81-101)}$ was synthesized and purified by reversed phase high-pressure liquid chromatography

†S.G. is grateful to the authority of Nanyang Technological University for awarding a research scholarship. This research was supported by A*STAR BMRC (08/1/22/19/576).

*To whom correspondence should be addressed. G.G.: telephone, +65-6316 2989; fax, +65-67913856; e-mail, ggrueber@ntu.edu.sg. C.V.: telephone, +65-6478 8273; fax, +65-64789045; e-mail, chandra@bii.a-star.edu.sg.

Published on Web 04/08/2010

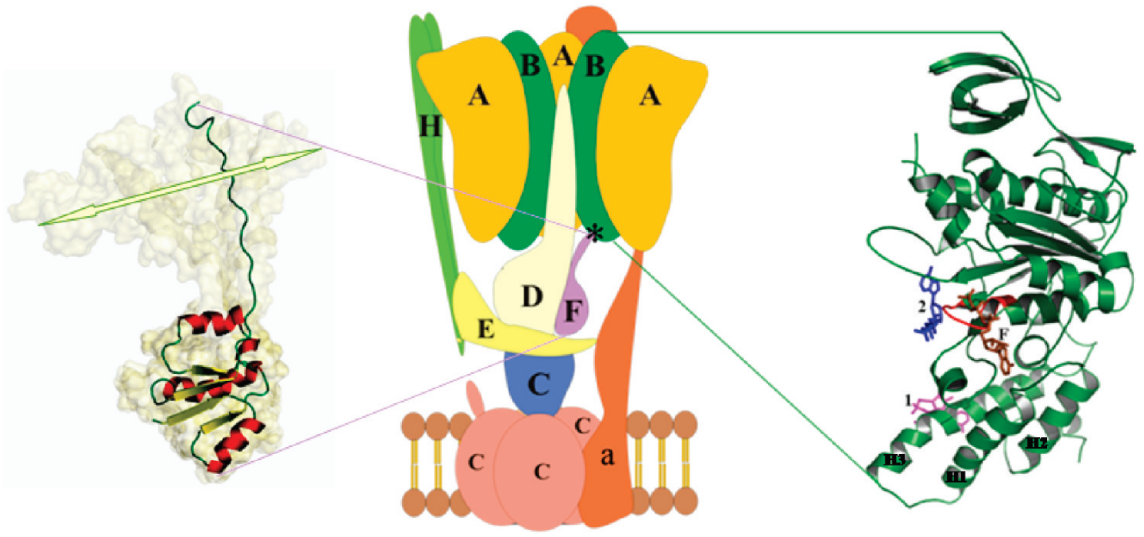

FIGURE 1: Arrangement of subunits in the A_1A_O ATP synthase. One B subunit has been removed from the A_1 section to reveal the D subunit (colored white) within the A_3B_3 headpiece. The asterisk indicates the region, forming a cross-link between the C-terminal end of subunit B and the elongated C-terminal end of subunit F. At the left is a ribbon diagram of the NMR structure of subunit F from *M. mazei* Gö1 A-ATP synthase inside an envelope, representing the conformational mobility of the C-terminus of F_{Mm}, as derived from backbone dynamics and two-dimensional $^1H-^{15}N$ heteronuclear NOE experiments. The cartoon representation (right) shows the transition I (1) and II position (2) as well as the final nucleotide-binding side (*F*) inside B_{Mm}. Mobile helices H1−H3 at the C-terminal end of B_{Mm} are denoted.

(HPLC) at the Division of Chemical Biology and Biotechnology, School of Biological Sciences, Nanyang Technological University. The purity and identity of the peptides were confirmed by HPLC and ESI-MS.[1]

NMR Spectroscopy. We prepared $F_{Mm(81-101)}$ by dissolving the peptide in 25 mM phosphate buffer (pH 6.8). All spectra were recorded at 288 K on a 600 MHz Avance Bruker NMR spectrometer. TOCSY and NOESY spectra of the peptide were recorded with mixing times of 80 and 300 ms, respectively. TopSpin (Bruker Biospin) and the Sparky (*14*) suite of programs were used for spectral processing, visualization, and peak picking. Standard procedures based on spin system identification and sequential assignments were adopted to identify the resonances (*15*). Dihedral angle restraints as derived from TALOS (*16*) were employed to generate the three-dimensional structure of the peptide in CYANA version 2.1 (*17*). In total, 100 structures were calculated. An ensemble of 20 structures with the lowest total energy was chosen for structural analysis. Secondary structure prediction using ^{13}C, ^{15}N, and ^1H chemical shifts of $F_{Mm(81-10)}$ was conducted with PREDITOR (*18*).

Molecular Modeling. The crystal structure of B_{Mm} is available in the Protein Data Bank (PDB) as entry 2C61 (*19*) at a resolution of 1.5 Å. There was no interpretable electron density for residues between E58 and I70. The missing region was modeled using the Modeller (*29*−*31*) suite of programs. This completed model of B_{Mm} and the 10 best NMR-derived structures of F_{Mm} with PDB entry 2OV6 (*13*) were used as starting coordinates.

APBS (*20*) together with the CHARMM force field (*21*−*23*) was used to compute electrostatic potential maps that were viewed with PyMOL (*24*). Modeling was conducted under conditions close to physiological ones, i.e., a temperature of 300 K and an ionic strength of 0.15 M. A solvent dielectric of 80 and a solute dielectric of 2 were used.

The structure of subunit A of *M. mazei* Gö1 was modeled on the basis of the crystal structure of homologous subunit A of *Pyrococcus horikoshii* OT3 (PDB entry 1vdz) using Modeller (*29*−*31*), with which it shared ~65% sequence similarity.

Docking. The $B_{Mm}-F_{Mm}$ assembly was modeled using HADDOCK (*25*, *26*), which allows for the integration of biochemical cross-linking and tryptophan fluorescence spectroscopy data as distance restraints to guide the docking. A total of 14 AIR's, describing the interactions between the $_{390}$EALSERDTK$_{399}$ region of B_{Mm} and the $_{88}$REKIK$_{92}$ region of F_{Mm} with an upper distance limit of 3 Å and one unambiguous distance restraint between W100 of F_{Mm} and W439 of B_{Mm} with an upper distance bound of 5 Å, were used for the docking. The definition of ambiguous interaction restraints was described in detail in ref *26*. An initial round of docking was conducted to study the interaction of $F_{Mm(81-101)}$ in its retracted and elongated forms with B_{Mm}. Four cases were considered; cases 1 and 3 dealt with the docking of the elongated $F_{Mm(81-101)}$ with B_{Mm}, and cases 2 and 4 employed the retracted form. The backbone and the side chain atoms of $F_{Mm(81-101)}$ were allowed to move freely in cases 1 and 2, while the backbone was restrained (to preserve the secondary structure) in cases 3 and 4. This preliminary docking was used to investigate the conformational preferences of F_{Mm} in its interactions with B_{Mm}. Subsequently, a final round of docking between B_{Mm} and elongated F_{Mm} restrained against data derived from biochemical cross-linking and intrinsic tryptophan fluorescence spectroscopy was performed. The HADDOCK protocol consisted of three stages. The first stage involved the generation of 1000 initial structures after randomization of orientations followed by energy minimization. The second stage involved semiflexible simulated annealing in torsion angle space in which the side chains and backbone atoms of the residues at and surrounding the interface were allowed to move freely and, finally, a third stage of refinement in explicit solvent in Cartesian space. Scoring and clustering

[1]Abbreviations: NMR, nuclear magnetic resonance; NOESY, nuclear Overhauser effect spectroscopy; TOCSY, total correlation spectroscopy; FRET, fluorescence resonance energy transfer; ESI-MS, electrospray ionization mass spectrometry; DSP, dithiobissulfosuccinimidyl propionate; EDC, 1-ethyl 3-[(dimethylamino)propyl]carbodiimide; AIR, ambiguous interaction restraints; R_1, longitudinal relaxation time; R_2, transverse relaxation time; MD, molecular dynamics; rmsd, root-mean square deviation; rmsf, root-mean square fluctuation; PCA, principal component analysis.

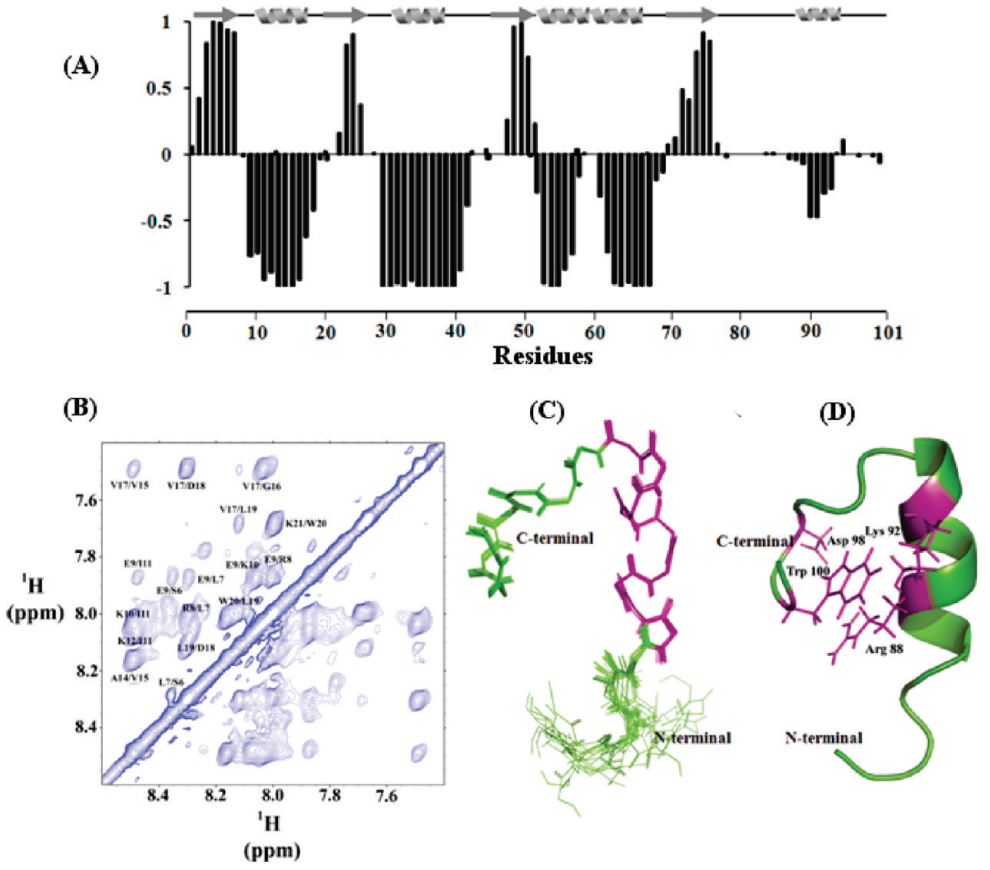

FIGURE 2: (A) Secondary structure prediction using chemical shift for subunit F from *M. mazei* Gö1. (B) HN−HN region of the NOESY spectra of $F_{Mm(81-101)}$. (C) Superimposition of the 20 lowest-energy structures of peptide $F_{Mm(81-101)}$. (D) Cartoon representation of a single $F_{Mm(81-101)}$ structure showing orientations of R88, K92, D98, and W100 side chains.

based on restraint violations and visual inspection allowed us to choose the best structure for further investigation through molecular dynamics simulations.

Molecular Dynamics Simulations. Molecular dynamics simulations were conducted using the CHARMM force field (*21*−*23*), using two different representations of solvent water. The explicit water simulations employed the TIP3 (*27*) model of water and were conducted using NAMD (*28*), while the simulations employing the continuum representation of bulk solvent were conducted using CHARMM (*29*).

Addition of Na^+ and Cl^- ions to the periodic box filled with water ensured that explicit simulations compensated for the net charges on B_{Mm}, F_{Mm}, and the B_{Mm}−F_{Mm} assembly. The electrostatic interactions were modeled using the particle mesh Ewald (*30*) summation method, and van der Waals energies were computed with a smooth (10−12 Å) cutoff. Following 2000 steps of initial minimization, each system was heated over 100 ps to 300 K. Equilibration over 400 ps and production runs over 10 ns with an integration time step of 1 fs were performed in the NpT ensemble using the Nose-Hoover Langevin piston pressure control (*31*, *32*) in NAMD.

The electrostatics in the continuum representation of the bulk solvent were modeled on the GBSW (*33*) function implemented in CHARMM. A self-consistent force field optimized for such solvent models (available as radius_gbsw.str and par_all27_prot_na_gbsw.inp) was utilized to compare the behavior of the elongated and helical forms of $F_{Mm(81-101)}$ (*33*). A grid spacing of 1.5 Å, a nonbond cutoff of 16 Å, and an integration time step of 2 fs were employed. Shake was used to hold all hydrogen bond distances near their equilibrium values. Each system was put through an identical protocol consisting of 500 steps of steepest descent minimization followed by 500 steps of minimization implementing the adopted basis Newton−Raphson method. Next, the system was equilibrated over 500 ps before 100 ns of production runs ensued. Analysis was conducted using CHARMM (*29*) and Wordom (*34*). Enthalpies were computed using the MM-GB (*35*−*37*) protocol with the temperature set to 300 K and the salt concentration set to 0.15 M.

RESULTS

Structure and Dynamics of F_{Mm} and $F_{Mm(81-101)}$. The NMR solution structure of F_{Mm} exhibits a distinct two-domain feature with a globular 78-residue N-terminus flexibly linked to an elongated C-terminus, formed by residues 79−101 (*13*). Backbone dynamics, as revealed by R_1, R_2, and two-dimensional (2D) ^{1}H−^{15}N heteronuclear NOE experiments on F_{Mm}, had previously indicated that residues 79−101 experience conformational mobility (*13*). Secondary structure predictions derived from chemical shifts of F_{Mm} reveal a propensity to form a helical structure across residues 86−94 (Figure 2A). The flexible C-terminal region of F_{Mm} is known to form a nucleotide-dependent zero-length cross-link with B_{Mm} via the peptide sequence $_{88}$REKIK$_{92}$ (*12*) and exists in an elongated form. To gain deeper insight into the solution behavior of this region, the NMR solution structure of the 21-mer $_{81}$GSGSTSLREKIKQAVGVDLWK$_{101}$ region, called $F_{Mm(81-101)}$, has been determined. Using standard procedures for sequential assignment based on homonuclear TOCSY and NOESY experiments (*15*), all the residues of the peptide were assigned (Figure 2B). Secondary structure predictions using the ^{1}H chemical shifts are

shown in Figure S1A of the Supporting Information. The connectivity diagram of the peptide is indicative of a helical conformation with the sequential HN−HN, H−HN (i, $i + 3$), H−HN (i, $i + 4$), and H−H (i, $i + 3$) connectivity (Figure S1B of the Supporting Information). Figure 2C shows an overlay of the 20 lowest-energy structures of the peptide, which have an overall root-mean-square deviation (rmsd) of 0.339 ± 0.31 Å. All these structures have energies lower than −100 kcal/mol, no NOE violations greater than 0.3 Å, and no dihedral violations greater than 5° (Table 1). $F_{Mm(81-101)}$ displays a short flexible N-terminal tail of amino acids G81−T85 and a helical motif formed by residues S86−A94 (Figure 2D), which is similar to the predicted 2D structure of F_{Mm} (Figure 2A).

To investigate the relative stabilities of F_{Mm} in the currently determined retracted helical form [henceforth termed $F_{Mm(81-101)}$] and of the previously determined elongated form F_{Mm} (*13*), we performed 100 ns molecular dynamics (MD) simulations on both structures using the continuum representation of bulk solvent water (*33*). The conformational change in terms of the rmsd of the C-termini of F_{Mm} and $F_{Mm(81-101)}$ (Figure S2A of the Supporting Information) relative to the structures used to initiate the simulations shows that $F_{Mm(81-101)}$ remains stable at ∼5 Å in contrast to the elongated C-terminus of F_{Mm}, which exhibits a value of ∼12.5 Å. The atomic fluctuations (rmsf) (Figure S2B of the Supporting Information) show that there is an almost 2-fold higher mobility among residues 86−94 of F_{Mm} when elongated than when retracted and helical. In addition, the solution structure of $F_{Mm(81-101)}$ reveals two cation−π interactions (*38*−*40*): one arising as a result of contacts between conserved R88 and W100 and a second between K92 and W100 (Figure 3A). During the simulations, the distance between R88 and W100 and between K92 and W100 varies between 5 and 15 Å for the retracted and elongated states, respectively (Figure 3B,C). Together, these observations highlight the intrinsic flexibility of the C-terminus. During the simulation, F_{Mm} collapses to an $F_{Mm(81-101)}$-like form but is very mobile. Similarly, $F_{Mm(81-101)}$ exhibits mobility that suggests a propensity for extension (movie1 of the Supporting Information). This suggests that the peptide has high intrinsic flexibility that would enable interconversions between the two forms, albeit at a time scale much longer than 100 ns.

Table 1: Structural Statistics for 21-mer Peptide from the C-Terminus of Subunit F

no. of distance restraints	
total	255
intraresidue ($i - j = 0$)	53
sequential ($\|i - j\| = 1$)	102
medium-range ($2 \leq \|i - j\| \leq 4$)	66
long-range ($\|i - j\| \geq 5$)	34
average no. of violations	
distance violations of > 5 Å	0
Ramachandran plot (%)	
residues in most favored regions	63.2
residues in additionally allowed regions	36.8
residues in generously allowed regions	0
residues in disallowed regions	0
average rmsd from the mean (Å)	
residues 3−21, backbone atoms (C^{α}, C′, and N)	0.339 ± 0.31

Structure of the B_{Mm}−F_{Mm} Assembly. Next, we characterized F_{Mm} in the context of a B_{Mm}−F_{Mm} assembly. Toward this end, we combined experimental data as restraints to build computational models as follows. Zero-length cross-link data (*12*) and intrinsic tryptophan fluorescence spectroscopy (*13*) showed that association of the B_{Mm}−F_{Mm} assembly occurs via their respective C-termini (Figure 1). More specifically, cross-linking with the reagent 1-ethyl 3-[(dimethylamino)propyl]carbodiimide (EDC) placed the $_{88}$REKIK$_{92}$ region of F_{Mm} and the $_{390}$EALSERTDK$_{399}$ region of B_{Mm} in the proximity of each other (*12*), while intrinsic fluorescence spectroscopy, performed on the wild-type and mutant samples $F_{MmW100Y}$, $F_{MmW100I}$, and B_{Mm}, showed that W100 of F_{Mm} and W430 of B_{Mm} interact with each other (*13*). To examine the forces that mediate this association, we analyzed the electrostatic surfaces of *M. mazei* Gö1 B_{Mm} and F_{Mm} (Figure 4). F_{Mm} is characterized by cationic regions on the extended C-terminus formed by residues R88, K90, K92, and Q93. In comparison, B_{Mm} has anionic patches on the ventral face spanning helix 1 (residues 395−409) and helix 2 (residues 422−435). These two complementary surfaces seem appropriately subtended to dock with each other. This arrangement also localizes a small cationic region on B_{Mm} (K410 and R420) to dock with an anionic region on the C-terminal face of F_{Mm} (D98). Such complementarity is absent on the dorsal face of B_{Mm}

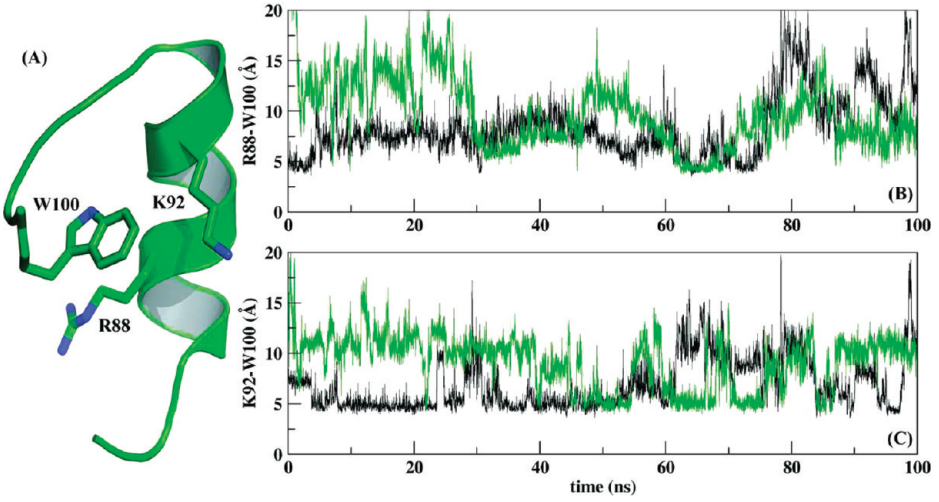

FIGURE 3: (A) Cation−π interactions in $F_{Mm(81-101)}$. The proximity of residues R88, K92 (a position that is always occupied by a positively charged residue such as K or R in subunit F across different species), and W100 is highlighted. (B) Distances between residues R88 and W100 and (C) distances between residues K92 and W100 mapped over 100 ns MD simulations for the retracted (black) and elongated (green) forms of $F_{Mm(81-101)}$.

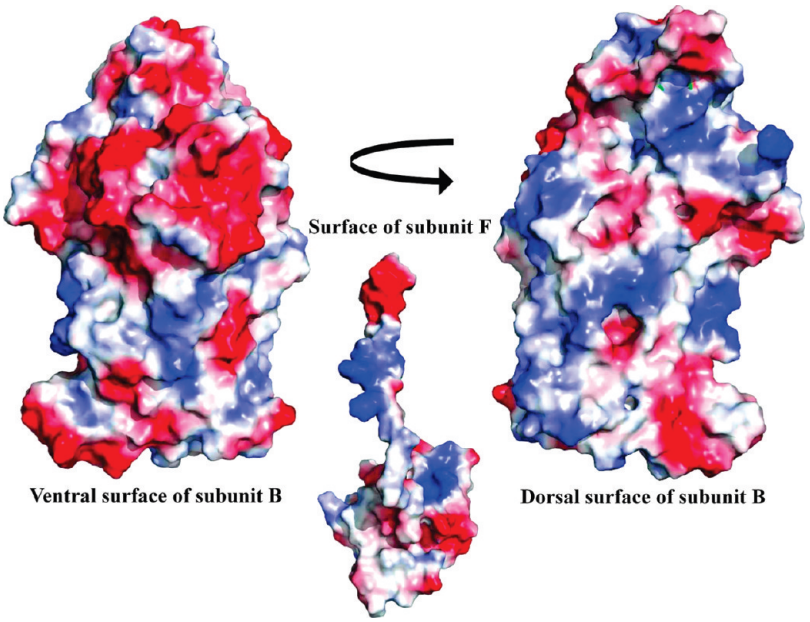

FIGURE 4: Electrostatic surfaces of B_{Mm} and F_{Mm} showing the favorable properties of the ventral surface of B_{Mm} with respect to the dorsal surface to bind F_{Mm}. The anionic regions are colored red, while the cationic regions are colored blue.

and leads us to conclude that the ventral surface of B_{Mm} is the most likely to bind with the extended C-terminus of F_{Mm}.

Using the characteristics described above, structures of the complex between B_{Mm} and F_{Mm} were modeled using HADDOCK (*25*, *26*).

To examine whether F_{Mm} adopted an extended or retracted form preferentially in its interactions with B_{Mm}, docking was initiated using both the retracted and elongated forms of $F_{Mm(81-101)}$. Four different scenarios as described in Materials and Methods were considered. The results (Figure S3 of the Supporting Information) revealed that only the elongated form of $F_{Mm(81-101)}$ could form interactions with B_{Mm} that were in accord with the experimental data [the violation energy of the restraints imposed together with the number of restraints violated in the retracted form of $F_{Mm(81-101)}$ exceeded those in the elongated form by ~3-fold]. Notably, the W100−W430 distance restraint derived from intrinsic tryptophan fluorescence spectroscopy was not shown to be satisfied in the models that resulted from the docking of the retracted form of $F_{Mm(81-101)}$. Additionally, when the backbone of the retracted form of $F_{Mm(81-101)}$ was left unrestrained during the docking, the best 10 structures lost their helicity and tended toward a more elongated arrangement. Taken together, this suggests that it is indeed the elongated form of F_{Mm} that interacts with B_{Mm}; consequently, the interaction of the retracted form of F_{Mm} and B_{Mm} was ignored for further study. A final round of docking between B_{Mm} and elongated F_{Mm}, restrained against data derived from biochemical cross-linking and intrinsic tryptophan fluorescence spectroscopy, was performed. The structure with the best energy profile and fewest restraint violations was chosen for further investigation.

The B_{Mm}−F_{Mm} complex is ~120 Å in length and ~50 Å in width (Figure 5A). Helices 1 and 2 of the C-terminus of B_{Mm} part by ~5 Å to accommodate the incoming elongated C-terminus of F_{Mm}. Electrostatic interactions between the pairs of side chains of R88 and E391, and K92 and E395, and between the backbone and side chains of R88 and K390, K90 and E395, and K92 and E402, respectively, satisfy the restraints as suggested by biochemical cross-linking data (*12*) (Figure 5B). The unambiguous distance

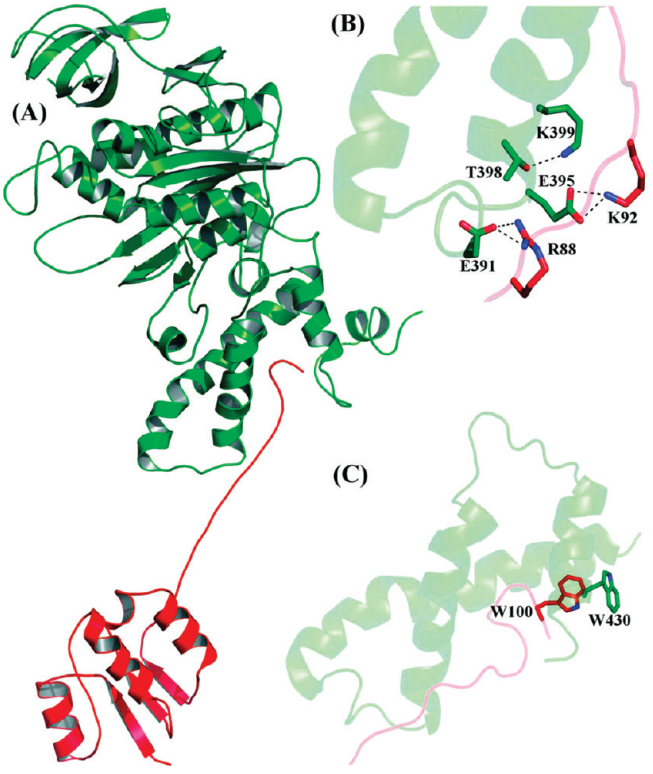

FIGURE 5: (A) Cartoon representation of the B_{Mm}−F_{Mm} assembly obtained with the Haddock protocol. B_{Mm} and F_{Mm} associate via their respective C-terminal ends. Restraints derived from (B) biochemical cross-linking between the $_{390}$EALSERDTK$_{399}$ region of B_{Mm} and the $_{88}$REKIK$_{92}$ region of F_{Mm} and (C) intrinsic fluorescence spectroscopy that places W100 of F_{Mm} and W430 of subunit B_{Mm} in the proximity of each other are well satisfied in our model.

restraint imposed between residue W100 of F_{Mm} and residue W430 of B_{Mm}, as derived from intrinsic fluorescence spectroscopy, is also satisfied with the residues separated by 3.5 Å (Figure 5C). The overall structures of the individual subunits remain well-conserved, with B_{Mm} and F_{Mm} of the complex within 0.4 Å and ~1 Å, respectively, of their positions in the initial structures.

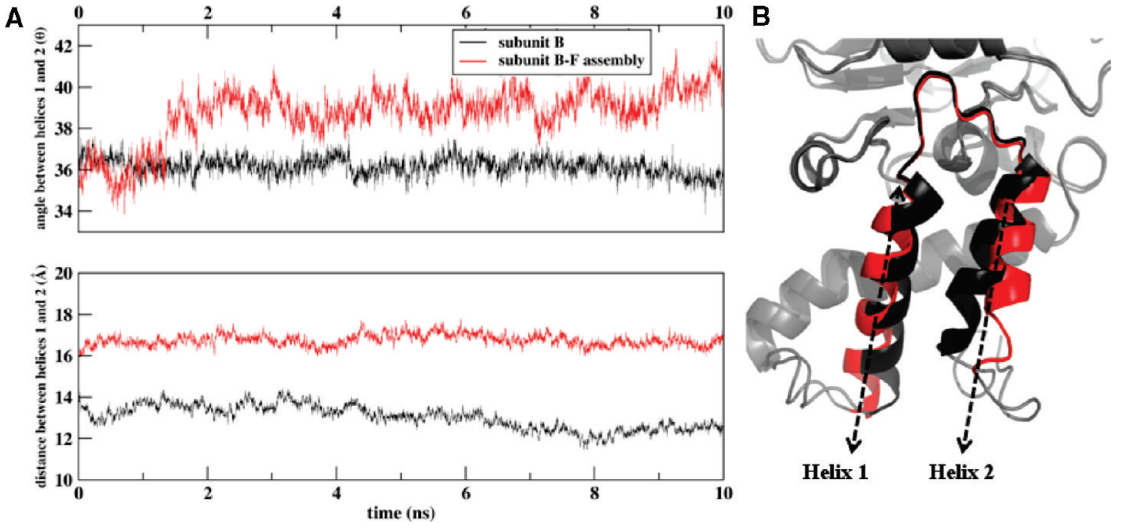

FIGURE 6: Dynamics of helices 1 and 2 in the C-terminus of the bound (red) and free (black) forms of B_{Mm}. (A) Variation of the angle between the two helices along the 10 ns molecular dynamics simulation which was derived as a dot product of the vectors arising between the C^{α} atoms of residues E395 and N417 and the other between the C^{α} atoms of residues N417 and H435. (B) Variations of the distance between the centers of masses of the two helices over 10 ns molecular dynamics simulations.

Structural Stability of B_{Mm}, F_{Mm}, and the B_{Mm}−F_{Mm} Assembly. Next we conducted molecular dynamics simulations on the B_{Mm}−F_{Mm} assembly. These simulations revealed that the experimental restraints employed to model the B_{Mm}−F_{Mm} complex remained satisfied over the conformational space sampled by our trajectories. The stability of the biochemical restraints between the $_{88}$REKIK$_{92}$ region of F_{Mm} and the $_{390}$EALSERTDK$_{399}$ region of B_{Mm} is seen in Figure S4 of the Supporting Information, showing that residues R88 and E391 (in red) and residues K92 and E395 (in green) of B_{Mm} and F_{Mm}, respectively, remain within ~4 Å of each other. The complexation also leads to the formation of polar contacts between residue E402 of B_{Mm} and residues R88 and K90 of F_{Mm}. Earlier work using intrinsic tryptophan fluorescence spectroscopy on F_{Mm} had shown that W100 is spatially close to residue W430 of B_{Mm} (*13*). We utilized this information in the initial model building by defining a distance-based restraint that held these two residues within 3.5 Å of each other. During the simulations, these residues remained within 3 Å of each other. The angle between the aromatic rings of the tryptophan residues was 44−46° (inset of Figure S4 of the Supporting Information). Furthermore, B_{Mm} can be divided into two main domains, one spanned by residues between positions 11 and 358 (an amalgamation of the N-domain and the α*β*-domain) and the other, the C-terminal domain (residues 359−460). A similar domain classification is followed for F_{Mm}, which consists of the globular N-terminus (residues 1−78) and residues 79−100 that make up the elongated C-terminus. Figure S5A of the Supporting Information reveals that in the uncomplexed state, B_{Mm} functions as a single unit with the rmsd of the C- and N-termini coalescing over 10 ns (shown as solid lines in black and red). In contrast, when B_{Mm} and F_{Mm} are bound to each other, a differential dynamics can be observed (shown with dotted lines). The plot reveals that the C-terminus of B_{Mm} undergoes more changes than the N-terminal region does, which remains relatively stable over the 10 ns. This arises because it is only the C-terminal region of B_{Mm} that binds to the C-terminus of F_{Mm}.

Relative orientations of helices 1 and 2 in B_{Mm} change from ~36° when uncomplexed to ~40° in the B_{Mm}−F_{Mm} assembly (Figure 6A). This is also accompanied by an increased parting of ~5 Å upon complexation (Figure 6B) to accommodate the incoming C-terminus of F_{Mm}. The rmsf of B_{Mm} mirrors the *B* value (*41*) distribution during the dynamics of the uncomplexed and complexed states. The amplitudes are lower in the crystal form as expected, because the motions are attenuated by crystal contacts and the protein forms a dimer in the crystallographic unit cell. The amplitudes of motion during the simulation are higher across B_{Mm} in its bound state but are particularly prominent in the N- and C-terminal regions (Figure S6A−C of the Supporting Information). Covariance among the fluctuations of the bound and free forms of B_{Mm} shows that in the uncomplexed form, the α*β*-region is more coherent as a domain than upon complexation (Figure S7 of the Supporting Information). As expected, upon complexation, the C-terminal region moves generally in a more negatively correlated manner relative to other parts of the protein. However, the general patterns of mobility are very similar between the two states (Figure S7 of the Supporting Information). The presence of domain motions became apparent when the fluctuations of each domain were examined separately (Figure S8 of the Supporting Information). It becomes obvious that in contrast to the unbound state, where the differences are small and localized to the C-terminal end, the bound state clearly shows a marked reduction in mobilities of both domains. Taken together, these data reveal that the two domains of B_{Mm} move as coherent correlated units upon complexation with F_{Mm}.

PCA was performed on the C^{α} atoms to isolate the dominant motions of B_{Mm} in its free and assembled forms. It is clear that the top three eigenvectors account for >60% of the overall fluctuations (Figure S9 of the Supporting Information). Some attenuation of motion, as expected upon complexation in general, is seen in the bound form along PC2 with a contribution at 14% (in contrast, the free form contributes 18%). The coverage of phase space along PC1 and PC2 suggests that while the free form is largely diffusive, upon complexation, the system hops across multiple minima (inset of Figure S9 of the Supporting Information). PC1 shows a negatively correlated motion of the two helices that define the binding site of the C-terminus of F_{Mm} (movie2 of the Supporting Information). Porcupine plots show that the unbound form of B_{Mm} (Figure 7A,B) has anticorrelated

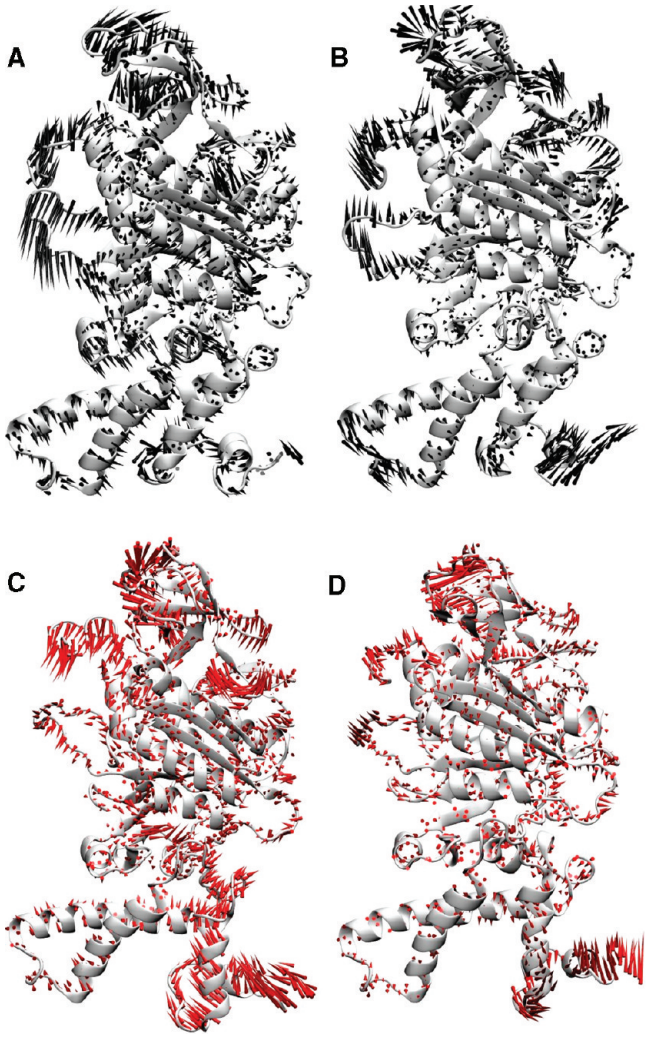

FIGURE 7: Schematic "porcupine plot" diagram of the major movement of domains captured during the 10 ns simulations of the free (black) and F_{Mm}-bound (red) forms of B_{Mm}. The lengths of the cones represent the amplitude of the fluctuations, while their orientation indicates the direction of motion of the C^{α} atom to which they are attached. (A and B) Motions along the first and second principal components, respectively, of the unbound form of B_{Mm}. (C and D) Motions along the first and second principal components, respectively, of the F_{Mm}-bound form of B_{Mm}.

motions between the two helices. In contrast, this motion changes in the bound state to a more correlated one, and the motion of helix 1 is dampened (Figure 7C,D). This damping occurs because F_{Mm} interacts more with helix 1 (Figure S10 of the Supporting Information). This favored interaction is largely electrostatic in origin (inset of Figure S10 of the Supporting Information). The amplitude of motion of helix 2, located at the C-terminal end of B_{Mm}, is much larger in the bound state. This is reminiscent of the kind of motions associated with peptide binding and egress. To search for a similar mode in the uncomplexed state, we examined the dot products of the vector associated with PC1 of the B_{Mm}–F_{Mm} assembly and all the vectors associated with the various PCs of the unbound form of B_{Mm}. Unfortunately, this motion was not apparent in the large amplitude region, and it is possible that it is much damped and hence appears at the high-frequency end. This suggests that the binding event may be triggered by the initial encounter between the C-terminus of the subunits, and this may "catalyze" the negatively correlated motions of the helices at the C-terminal end of B_{Mm}, to enable the eventual binding of the elongated C-terminus of F_{Mm}. Hydrogen bond analysis reveals that in the unbound form, the interhelical contact is dominated by two interactions: one between the side chains of E402 and H435 and the other between the side chains of K410 and Q431. These two interactions are disrupted upon F_{Mm} binding, which causes these residues to move beyond hydrogen bonding distance. Consequently, new intermolecular hydrogen bonds, mostly localized between F_{Mm} and helix 1, that serve to overcompensate for the earlier loss are formed. The intermolecular interactions of note arise between the side chains of R88 and E391, R88 and E402, K90 and E402, K92 and E395, K101 and Q440, and V95 and K399 and between the backbone and side chains of R88 and K390, K90 and E395, K90 and T398, and K101 and G442. The interaction between the helices is smaller as expected when parted. With the overall fluctuations of B_{Mm} remaining largely unchanged (rmsf averaged over all non-hydrogen atoms of ~1.4 Å for both the unbound and F_{Mm}-bound form of B_{Mm}) and those of F_{Mm} undergoing a significant reduction (the rmsf averaged over all non-hydrogen atoms for F_{Mm} decreases from 6.7 to 3.3 Å upon binding with B_{Mm}), it is clear that a large entropic penalty is associated with formation of the complex. This is a qualitative analysis, because a quantitative estimate will involve far more complex processes such as the release of water molecules and ions and is beyond the scope of this study. In addition, the strain associated with both subunits increases on complexation [the overall enthalpies of F_{Mm} change from −1994 to −1911 kcal/mol upon complexation (with a standard deviation of ~30 kcal/mol), and that of B_{Mm} changes from −9209 to −9095 kcal/mol (with a standard deviation of ~65 kcal/mol)]. This large penalty is compensated by the various interactions that are formed between the two subunits that are listed above (indeed, the enthalpy of the complex is −11092 kcal/mol, with a standard deviation of 70 kcal/mol, thus leading to a net compensation of ~85−170 kcal/mol). It is clear that this binding energy comes largely from the interactions of F_{Mm} with helix 1 (Figure S1 of the Supporting Information).

DISCUSSION

NMR and computational studies on $F_{Mm(81-101)}$ and F_{Mm} have extended previous work (*13*) and suggest that this domain is conformationally heterogeneous, spanning a retracted and extended state. Simulations reproduce the secondary structural aspects determined by NMR and suggest that interconversions occur on time scales much longer than those simulated. The C-terminal alterations of F_{Mm} are reflected by its nucleotide-dependent cross-link formation with B_{Mm} as shown in the A_3B_3DF complex and the A_1A_O ATP synthase from *M. mazei* Gö1 (*4*, *11*) and *Methanococcus jannaschii* (*12*), independent of whether DSP or the zero-length EDC was used. The zero-length cross-link is formed with the C-terminal $_{388}$DLVAVV-GEEALTDR$_{401}$ region of B_{Mm} (*12*), which is at a position similar to that of the so-called DELSEED region of nucleotide-binding subunits α and *β* of the F_1F_O ATP synthases, forming a disulfide bond with the C-terminal helix of subunit *ε* (*42*, *43*). Like F_{Mm}, the coupling subunit *ε* has been shown to be in an extended (*44*, *45*) conformation, bringing the C-terminus into the proximity of the DELSEED region of nucleotide-binding subunit α or *β* (*42*), and in a relaxed (*46*) structure. Furthermore, chemical modification of subunit *ε* of *Escherichia coli* F-ATP synthase indicated that the C-terminal domain is intrinsically

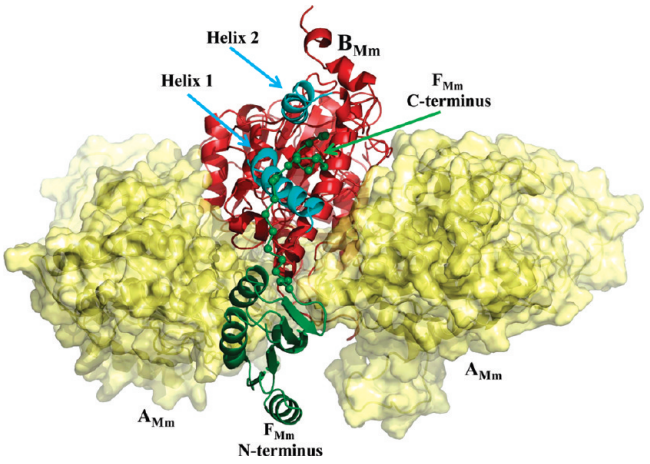

FIGURE 8: Assembly of the quaternary complex of the $B_{Mm}-F_{Mm}$ assembly and two A subunits of the hexameric headpiece. Subunit A of *M. mazei* Gö1 was modeled on the previously determined X-ray crystal structure of subunit A of *Pyrococcus horikoshii* [PDB entry 1vdz (*57*)] with which it shared ~65% sequence similarity. Then two molecules of subunit A and the $B_{Mm}-F_{Mm}$ complex of *M. mazei* Gö1, derived from this study, were juxtaposed on a previously published model (*13*) that was fitted into the electron density maps of the A_1 ATPase and the A_1A_O ATP synthase obtained from single-particle analysis electron micrographs. Subunits B and F are colored red and green, respectively, and shown as cartoons, while the surface of the two forms of subunit A are colored yellow. Helices 1 and 2 of B_{Mm} that part to accommodate the incoming C-terminus of F_{Mm} are colored cyan.

flexible (*47*, *48*). Together with cross-linking (*47*−*49*) and FRET experiments (*48*), these studies have revealed that the extended state of subunit ε inhibits ATP hydrolysis and restricts the rotation of subunit γ to which subunit ε is connected via its N-terminal domain (*50*−*52*). Cross-linking by EDC also showed that F_{Mm} of the methanogenic A-ATP synthase is in close contact with stalk subunits C and D (*12*). By comparison, the N-terminal domain of F (F_{Mm}) is in the proximity of the proposed rotary subunit D and the central bottom subunit C of A-ATP synthases, as demonstrated by cross-link formations using EDC (*4*, *11*, *12*). In summary, we suggest that the globular part of F_{Mm} emerges from the bottom domain of the central stalk of A_1, where it interacts with both subunits C and D, and goes up until the extended C-terminus of F_{Mm} reaches its assembly partner, B_{Mm}, for crosstalking in the A_1 headpiece; in contrast, the interaction of F_{Mm} in its retracted state with B_{Mm} is lost (Figure S11 of the Supporting Information).

To examine the extent of interaction between the retracted form of F_{Mm} and B_{Mm}, docking experiments, similar to those conducted as described above, were performed. It was clear that the restraint violation energy used as a filter was 3-fold higher for the retracted form than for the elongated form of F_{Mm}. Notably, the W100−W430 distance restraint derived from intrinsic tryptophan fluorescence spectroscopy was not shown to be satisfied in these models generated, and hence, the interaction between the retracted form of F_{Mm} and B_{Mm} was ignored for further study.

Electrostatics appear to direct the relative orientations of the two subunits with respect to each other during assembly. Simulations substantiate this by showing that these restraints are stable over the 10 ns simulation time scales. The C-terminal domain of F_{Mm} is encapsulated within the C-terminal domain of B_{Mm}. It is clear from covariance analysis that complexation leads to increased mobility at the C-terminus of B_{Mm}. It further shows that the perturbation induced by F_{Mm} upon association is localized to the C-terminus of B_{Mm}. To put our models of the $B_{Mm}-F_{Mm}$ complex in the context of the larger assembly of the A-ATP synthases, we constructed an assembly in which the structure of free B_{Mm} and its complex with F_{Mm} were fitted between two A subunits, like in the hexameric headpiece. It is clear from Figure 8 that both helix 1 and helix 2 are not involved in any contacts with the neighboring A subunits. Moreover, the highly mobile helix 2 is projected out toward solvent, away from any direct contacts. This suggests that the motions of B_{Mm}, which are coupled to the complexing F_{Mm}, would occur without a major influence from the neighboring subunits in the context of the larger hexameric assembly. Principle component analysis reveals that prior to complexation, the system is diffusive in its mobility while upon formation of the $B_{Mm}-F_{Mm}$ complex, the system seems to hop across minima. The complexity of such motions is further revealed through the porcupine plots, which show how the system moves as two domains that can be separated by a plane between the loops containing R263 and D309. Upon assembly of the $B_{Mm}-F_{Mm}$ complex, the plane of demarcation changes to that defined previously between the N- and C-terminal regions. It becomes obvious from the porcupine plots and detailed analysis that, upon binding, the major perturbation is spread through the hinge regions and involves changes between charge−charge and charge−dipole interactions spreading to the N-terminal domain. Examples are the change in the E331−R379 salt bridge to an E331−R334 salt bridge as well as the interactions of R330 with D308, and nearby backbone atoms change upon binding of F_{Mm} to the backbone of a spatially contiguous loop, containing the backbone of S152. In addition, an interaction between the R349 side chain and the backbone of T322 is lost, leading to a movement of E323 that in turn loses a hydrogen bonded to the side chain of Y284, and that in turn leads through a series of domino effect changes to a repositioning of the two loops (containing R269 and R379).

Interestingly, most of these residues are conserved across the A- and F-ATP synthases (*53*), suggesting an additional pattern of conservation through intramolecular dynamics. Overall, an entropic penalty is paid for the reduction of the mobility of F_{Mm} as it embeds in between helices 1 and 2 of B_{Mm}. This complexation also induces strain in both subunits. However, the interactions that ensue between the two subunits compensate for this penalty and drive the overall binding. Moreover, the mobilities of helices 1 and 2 in the C-terminal segment of B_{Mm} after assembly of the $B_{Mm}-F_{Mm}$ complex are in canon with a 6° movement of the C-terminal domain of B_{Mm}, including helices 1−3 (Figure 1), after binding of ATP to its so-called transition state 1, located between residues E377 and L381 of helix 3. It has been suggested that the binding of an ATP molecule in the transient I structure imposes a conformational change on the C-terminal domain by inducing a rotation of ~6° (*10*). As formation of cross-links between the C-termini of B_{Mm} and F_{Mm} occurs only in the presence of ATP, we propose that F_{Mm} is closely associated with B_{Mm} via their C-termini, and once the ATP enters, as in the transient I structure, the C-terminal domain of B_{Mm} rotates a bit, allowing the ATP molecule to penetrate inside the hexamer by moving into its transition state II position close to the P loop, before it binds to its final binding pocket (Figure 1). This concerted mobility is proposed to be linked with rotational movements of the central subunit D, connecting the events of ion pumping in A_O with nucleotide binding in the A_3B_3 catalytic headpiece.

Finally, we turn our attention to the robustness of the computational methods used, in particular the comparison between the two representations of the water environment: the explicit water simulations and the implicit water simulations.

Several lines of evidence have pointed out that while there is good general overall agreement over a range of tests such as computation of potentials of mean force (*54*), nevertheless caution needs to be exercised in interpretations even as progress is being made (*55*, *56*). For example, unsurprisingly, hydrogen bonds and salt bridges may be overstabilized in the continuum models since putative bridging water molecules are absent in these. In our work, the numbers of salt bridges for example differ by 20%. Further, the rmsd of the retracted form of $F_{Mm(81-101)}$ averages between 4.9 and 5.4 Å, with standard deviations ranging from 0.6 to 1 Å, when the simulation is conducted in explicit solvent (four simulations, each of 10 ns, with different initial conditions were performed). In contrast, the rmsd of the elongated form of $F_{Mm(81-101)}$ when computed over 10 windows of 10 ns each from the 100 ns simulation has an average between 5.2 and 6.2 Å, with standard deviations ranging from 0.3 to 0.9 Å. The two distributions suggest very similar behavior. At a closer level, we monitored the distributions of distances that define the existence of two cation$-\pi$ interactions: between R88 and W100 and between K92 and W100 (Figure S12 of the Supporting Information). It is clear that the first peak in the distributions, representing the close approach between the side chains, is very similar in the two cases; i.e., the absence of explicit water does not seem to have a significant effect. Clearly, these similarities suggest that the two representations of solvent yield descriptions that are similar and sufficient for the purposes of this study.

ACKNOWLEDGMENT

We thank Dr. Malathy S. S. Manimekalai (School of Biological Sciences, Nanyang Technological University) for helpful discussions.

SUPPORTING INFORMATION AVAILABLE

Twelve figures (Figures S1−S12) and two movies (movie1 and movie2) as described in the text. This material is available free of charge via the Internet at http://pubs.acs.org.

REFERENCES

1. Müller, V., and Grüber, G. (2003) ATP synthases: Structure, function and evolution of unique energy converters. *Cell. Mol. Life Sci. 60*, 474–494.
2. Grüber, G., and Marshansky, V. (2008) New insights into structure-function relationships between archaeal ATP synthase (A_1A_O) and vacuolar type ATPase (V_1V_O). *BioEssays 30*, 1096–1109.
3. Nelson, N. (1992) Evolution of organellar proton-ATPases. *Biochim. Biophys. Acta 1100*, 109–124.
4. Coskun, U., Radermacher, M., Müller, V., Ruiz, T., and Grüber, G. (2004) Three-dimensional organization of the archaeal A_1-ATPase from *Methanosarcina mazei* Gö1. *J. Biol. Chem. 279*, 22759–22764.
5. Grüber, G., Svergun, D. I., Coskun, U., Lemker, T., and Koch, M. H. J. (2001) Structural insights into the A_1 ATPase from the archaeon *Methanosarcina mazei* Gö1. *Biochemistry 40*, 1890–1896.
6. Coskun, Ü., Chaban, Y. L., Lingl, A., Müller, V., Keegstra, W., Boekema, E. J., and Grüber, G. (2004) Structure and subunit arrangement of the A-type ATP synthase complex from the archaeon *Methanococcus jannaschii* visualized by electron microscopy. *J. Biol. Chem. 279*, 38644–38648.
7. Bernal, R. A., and Stock, D. (2004) Three-dimensional structure of the intact *Thermus thermophilus* H^+-ATPase/synthase by electron microscopy. *Structure 12*, 1789–1798.
8. Vonck, J., Pisa, K. Y., Morgner, N., Brutschy, B., and Müller, V. (2009) Three-dimensional structure of A_1A_O ATP synthase from the hyperthermophilic archaeon *Pyrococcus furiosus* by electron microscopy. *J. Biol. Chem. 284*, 10110–10119.
9. Kumar, A., Manimekalai, M. S. S., Balakrishna, A. M., Hunke, C., Weigelt, S., Sewald, N., and Grüber, G. (2009) Spectroscopic and crystallographic studies of the mutant R416W give insight into the nucleotide binding traits of subunit B of the A_1A_O ATP synthase. *Proteins 75*, 807–819.
10. Manimekalai, M. S. S., Kumar, A., Balakrishna, A., and Grüber, G. (2009) A second transient position of ATP on its trail to the nucleotide-binding site of subunit B of the motor protein A_1A_O ATP synthase. *J. Struct. Biol. 166*, 39–45.
11. Coskun, U., Grüber, G., Koch, M. H. J., Godovac-Zimmermann, J., Lemker, T., and Müller, V. (2002) Cross-talk in the A_1-ATPase from *Methanosarcina mazei* Gö1 due to nucleotide binding. *J. Biol. Chem. 277*, 17327–17333.
12. Schäfer, I., Rossle, M., Biuković, G., Müller, V., and Grüber, G. (2006) Structural and functional analysis of the coupling subunit F in solution and topological arrangement of the stalk domains of the methanogenic A_1A_O ATP synthase. *J. Bioenerg. Biomembr. 38*, 83–92.
13. Gayen, S., Vivekanandan, S., Biuković, G., Grüber, G., and Yoon, H. S. (2007) NMR solution structure of subunit F of the methanogenic A_1A_O adenosine triphosphate synthase and its interaction with the nucleotide-binding subunit B. *Biochemistry 46*, 11684–11694.
14. Goddard, T. D., and Kneller, D. G. (2008) SPARKY 3, University of California, San Francisco.
15. Wüthrich, K. (1986) NMR of Proteins and Nucleic Acids, Wiley, New York.
16. Cornilescu, G., Delaglio, F., and Bax, A. (1999) Protein backbone angle restraints from searching a database for chemical shift and sequence homology. *J. Biomol. NMR 13*, 289–302.
17. Güntert, P., Mumenthaler, C., and Wüthrich, K. (1997) Torsion angle dynamics for NMR structure calculation with the new program DYANA. *J. Mol. Biol. 273*, 283–298.
18. Berjanskii, M. V., Neal, S., and Wishart, D. S. (2006) PREDITOR: A web server for predicting protein torsion angle restraints. *Nucleic Acids Res. 34*, 63–69.
19. Schäfer, I. B., Bailer, S. M., Düser, M. G., Börsch, M., Bernal, R. A., Stock, D., and Grüber, G. (2006) Crystal structure of the archaeal A_1A_O ATP synthase subunit B from *Methanosarcina mazei* Gö1: Implications of nucleotide-binding differences in the major A_1A_O subunits A and B. *J. Mol. Biol. 358*, 725–740.
20. Baker, N. A., Sept, D., Joseph, S., Holst, M. J., and McCammon, J. A. (2001) Electrostatics of nanosystems: Application to microtubules and the ribosome. *Proc. Natl. Acad. Sci. U.S.A. 98*, 10037–10041.
21. Mackerell, A. D., Jr. (2004) Empirical force fields for biological macromolecules: Overview and issues. *J. Comput. Chem. 25*, 1584–1604.
22. Mackerell, A. D., Jr., Banavali, N., and Foloppe, N. (2001) Development and current status of the CHARMM force field for nucleic acids. *Biopolymers 56*, 257–265.
23. Mackerell, A. D., Jr., and Nilsson, L. (2008) Molecular dynamics simulations of nucleic acid-protein complexes. *Curr. Opin. Struct. Biol. 18*, 194–199.
24. DeLano, W. L. (2002) The PyMOL Molecular Graphics System, DeLano Scientific, Palo Alto, CA.
25. de Vries, S. J., van Dijk, A. D., Krzeminski, M., van Dijk, M., Thureau, A., Hsu, V., Wassenaar, T., and Bonvin, A. M. (2007) HADDOCK versus HADDOCK: New features and performance of HADDOCK2.0 on the CAPRI targets. *Proteins 69*, 726–733.
26. Dominguez, C., Boelens, R., and Bonvin, A. M. (2003) HADDOCK: A protein-protein docking approach based on biochemical or biophysical information. *J. Am. Chem. Soc. 125*, 1731–1737.
27. Jorgensen, W. L., Chandrasekhar, J., Madura, J. D., Impey, R. W., and Klein, M. L. (1983) Comparison of simple potential functions for simulating liquid water. *J. Chem. Phys. 79*, 926–935.
28. Phillips, J. C., Braun, R., Wang, W., Gumbart, J., Tajkhorshid, E., Villa, E., Chipot, C., Skeel, R. D., Kale, L., and Schulten, K. (2005) Scalable molecular dynamics with NAMD. *J. Comput. Chem. 26*, 1781–1802.
29. Brooks, B. R.., Brooks, C. L., III, Mackerell, A. D., Nilsson, L., Petrella, R. J., Roux, B., Won, Y., Archontis, G., Bartels, C., Boresch, S., Caflisch, A., Caves, L., Cui, Q., Dinner, A. R., Feig, M., Fischer, S., Gao, J., Hodoscek, M., Im, W., Kuczera, K., Lazaridis, T., Ma, J., Ovchinnikov, V., Paci, E., Pastor, R. W., Post, C. B., Pu, J. Z., Schaefer, M., Tidor, B., Venable, R. M., Woodcock, H. L., Wu, X., Yang, W., York, D. M., and Karplus, M. (2009) CHARMM: The Biomolecular Simulation Program. *J. Comput. Chem. 30*, 1545–1615.
30. Darden, T., York, D., and Pederson, L. (1993) Particle Mesh Ewald: An $N\cdot\log(N)$ method for Ewald sums in large systems. *J. Chem. Phys. 98*, 10089–10093.
31. Martyna, G. J., Tobias, D. J., and Klein, M. L. (1994) Constant pressure molecular dynamics algorithms. *J. Chem. Phys. 101*, 4117–4189.
32. Feller, S. E., Zhang, Y., Pastor, R. W., and Brooks, B. R. (1995) Constant pressure molecular dynamics simulation: The Langevin piston method. *J. Chem. Phys. 103*, 4316–4621.

33. Im, W., Lee, M. S., and Brooks, C. L. (2003) Generalized Born model with a simple smoothing function. *J. Comput. Chem. 24*, 1691–1702.
34. Seeber, M., Cecchini, M., Rao, F., Settanni, G., and Caflisch, A. (2007) Wordom: A program for efficient analysis of molecular dynamics simulations. *Bioinformatics 23*, 2625–2627.
35. Kollman, P. A., Massova, I., Reyes, C., Kuhn, B., and Huo, S. H. (2000) Calculating structures and free energies of complex molecules: Combining molecular mechanics and continuum models. *Acc. Chem. Res. 33*, 889–897.
36. Srinivasan, J., Cheatham, T. E., Cieplak, P., Kollman, P. A., and Case, D. A. (1998) Continuum solvent studies of the stability of DNA, RNA, and phosphoramidate-DNA helices. *J. Am. Chem. Soc. 120*, 9401–9409.
37. Massova, I., and Kollman, P. A. (2000) Combined molecular mechanical and continuum solvent approach (MM-PBSA/GBSA) to predict ligand binding. *Perspect. Drug Discovery Des. 18*, 113–135.
38. Dougherty, D. A. (1996) Cation-π interactions in chemistry and biology: A new view of benzene, Phe, Tyr, and Trp. *Science 271*, 163–168.
39. Dougherty, D. A. (2007) Cation-π interactions involving aromatic amino acids. *J. Nutr. 137*, 1504–1508.
40. Gallivan, J. P., and Dougherty, D. A. (1999) Cation-π interactions in structural biology. *Proc. Natl. Acad. Sci. U.S.A. 96*, 9459–9464.
41. Willis, B. T. M., and Pryor, A. W. (1975) Thermal Vibrations in Crystallography, Cambridge University Press, New York.
42. Capaldi, R. A., Aggeler, R., Wilkens, S., and Grüber, G. (1996) Structural changes in the γ and ε subunits of the *Escherichia coli* F_1F_O-type ATPase during energy coupling. *J. Bioenerg. Biomembr. 28*, 397–401.
43. Aggeler, R., Chicas-Cruz, K., Cai, S. X., Keana, J. F., and Capaldi, R. A. (1992) Introduction of reactive cysteine residues in the ε subunit of *Escherichia coli* F_1 ATPase, modification of these sites with tetrafluorophenyl azide-maleimides, and examination of changes in the binding of the ε subunit when different nucleotides are in catalytic sites. *Biochemistry 31*, 2956–2961.
44. Wilkens, S., Dahlquist, F. W., McIntosh, L. P., Donaldson, L. W., and Capaldi, R. A. (1995) Structural features of the ε subunit of the *Escherichia coli* ATP synthase determined by NMR spectroscopy. *Nat. Struct. Biol. 2*, 961–967.
45. Rodgers, A. J., and Wilce, M. C. (2000) Structure of the γ-ε complex of ATP synthase. *Nat. Struct. Biol. 7*, 1051–1054.
46. Gibbons, C., Montgomery, M. G., Leslie, A. G., and Walker, J. E. (2000) The structure of the central stalk in bovine F_1-ATPase at 2.4 Å resolution. *Nat. Struct. Biol. 7*, 1055–1061.
47. Ganti, S., and Vik, S. B. (2007) Chemical modification of monocysteine mutants allows a more global look at conformations of the ε subunit of the ATP synthase from *Escherichia coli*. *J. Bioenerg. Biomembr. 9*, 99–107.
48. Schulenberg, B., and Capaldi, R. A. (1999) The ε subunit of the F_1F_O complex of *Escherichia coli* cross-linking studies show the same structure in situ as when isolated. *J. Biol. Chem. 274*, 28351–28355.
49. Iino, R., Murakami, T., Iizuka, S., Kato-Yamada, Y., Suzuki, T., and Yoshida, M. (2005) Real-time monitoring of conformational dynamics of the ε subunit in F_1-ATPase. *J. Biol. Chem. 280*, 40130–40134.
50. Zimmermann, B., Diez, M., Zarrabi, N., Gräber, P., and Börsch, M. (2005) Movements of the ε-subunit during catalysis and activation in single membrane-bound H^+-ATP synthase. *EMBO J. 24*, 2053–2063.
51. Tsunoda, S. P., Rodgers, A. J., Aggeler, R., Wilce, M. C., Yoshida, M., and Capaldi, R. A. (2001) Large conformational changes of the ε subunit in the bacterial F_1F_O ATP synthase provide a ratchet action to regulate this rotary motor enzyme. *Proc. Natl. Acad. Sci. U.S.A. 98*, 6560–6564.
52. Iino, R., Hasegawa, R., Tabata, K. V., and Noji, H. (2009) Mechanism of inhibition by C-terminal α-helices of the ε subunit of *Escherichia coli* F_OF_1-ATP synthase. *J. Biol. Chem. 284*, 17457–17464.
53. Olendzenski, L., Hilario, E., and Gogarten, J. P. (1998) in Horizontal gene transfer (Syvanen, K., and Kado, C. I., Eds.) pp 349−362, Chapman & Hall, New York.
54. Scarsi, M., Apostolakis, J., and Caflisch, A. (1998) Comparison of a GB Solvation Model with Explicit Solvent Simulations: Potentials of Mean Force and Conformation preferences of Alanine Dipeptide and 1,2-Dichloroethane. *J. Phys. Chem. B 102*, 3637–3641.
55. Simonson, T. (2001) Macromolecular electrostatics: Continuum models and their growing pains. *Curr. Opin. Struct. Biol. 11*, 243–252.
56. Chen, J., Im, W., and Brooks, C. L. (2006) Balancing Solvation and Intramolecular Interactions: Toward a Consistent Generalized Born Force Field. *J. Am. Chem. Soc. 128*, 3728–3736.
57. Maegawa, Y., Morita, H., Iyaguchi, D., Yao, M., Watanabe, N., and Tanaka, I. (2006) Structure of the catalytic nucleotide-binding subunit A of A-type ATP synthase from *Pyrococcus horikoshii* OT3 reveals a novel domain related to the peripheral stalk. *Acta Crystallogr. D62*, 483–488.